

Supporting Information

Trends in Competing Oxygen and Chlorine Evolution Reactions over Electrochemically Formed Single-Atom Centers of MXenes

Shohreh Faridi¹, Samad Razzaq¹, Diwakar Singh¹, Ling Meng², Francesc Vines²,
Francesc Illas², Kai S. Exner^{1,3,4,*}

¹ *University of Duisburg-Essen, Faculty of Chemistry, Theoretical Catalysis and Electrochemistry, Universitätsstraße 5, 45141 Essen, Germany*

² *Departament de Ciència de Materials i Química Física & Institut de Química Teòrica i Computacional (IQTCUB), Universitat de Barcelona, c/ Martí i Franquès 1-11, 08028 Barcelona, Spain*

³ *Cluster of Excellence RESOLV, 44801 Bochum, Germany*

⁴ *Center for Nanointegration (CENIDE) Duisburg-Essen, 47057 Duisburg, Germany*

* Corresponding author: kai.exner@uni-due.de ORCID: 0000-0003-2934-6075

1 Electronic structure of MXene-SAC sites

To gain insight into the electronic structure of the MXene-SAC sites, we have calculated the density of states (DOS) for selected MXene-SAC motifs. The DOS for Hf₂C-SAC, Zrf₂C-SAC, Ti₂C-SAC, and Mo₂C-SAC is provided in **Figures S1-S4**, respectively.

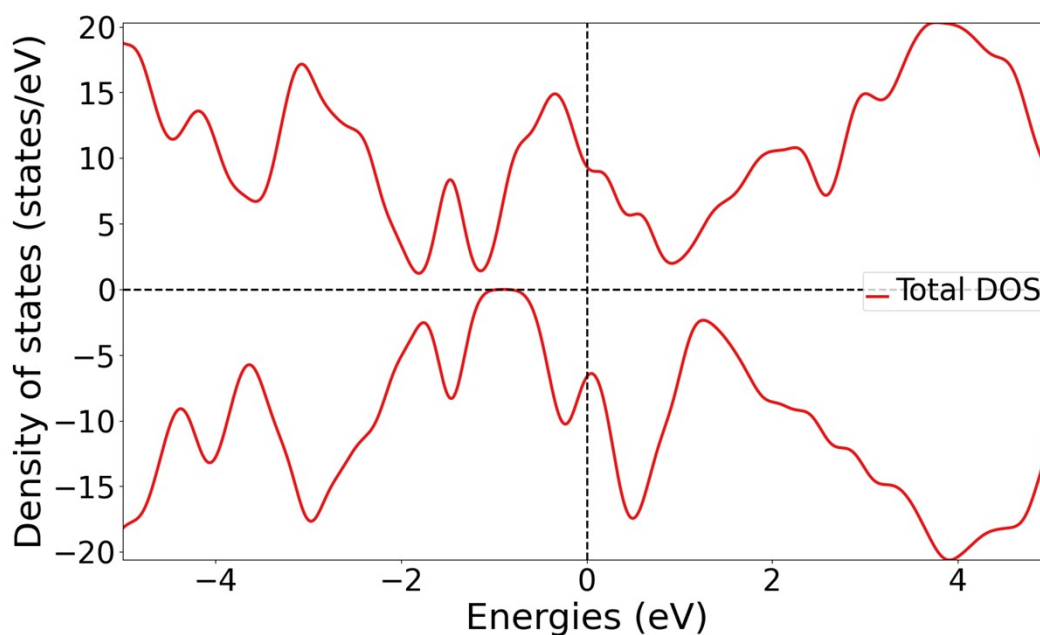


Figure S1. Density of states for Hf₂C-SAC.

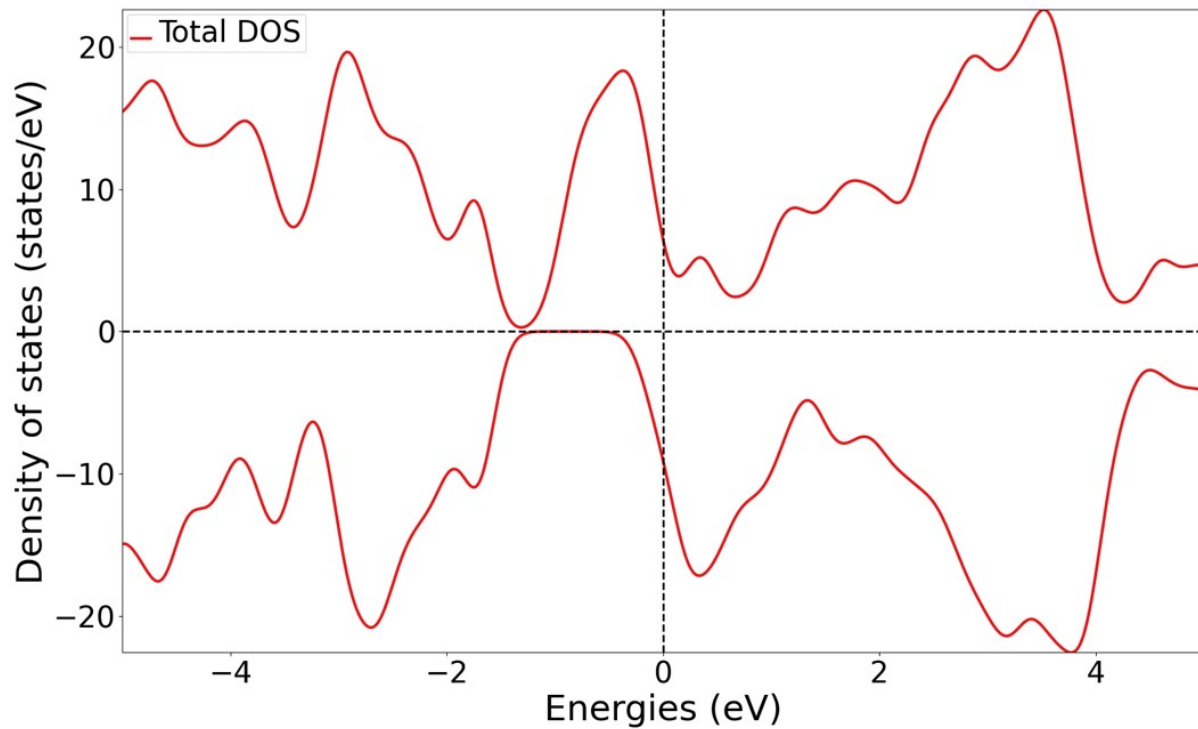


Figure S2. Density of states for Zr₂C-SAC.

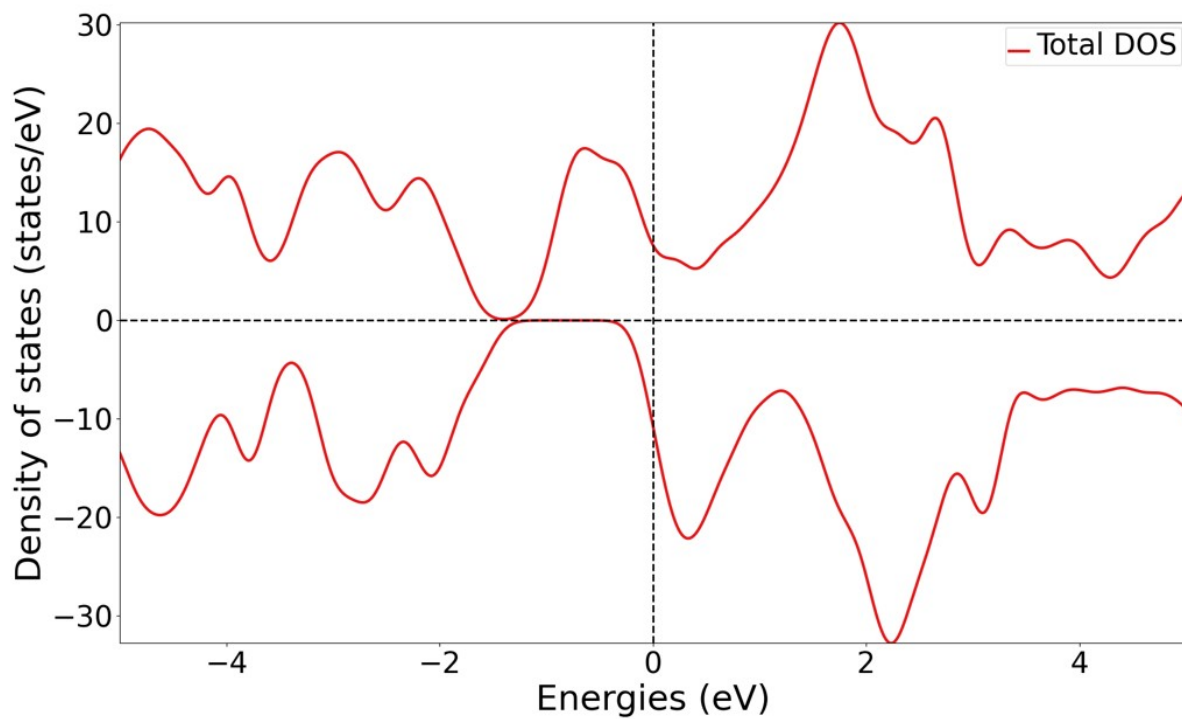


Figure S3. Density of states for Ti₂C-SAC.

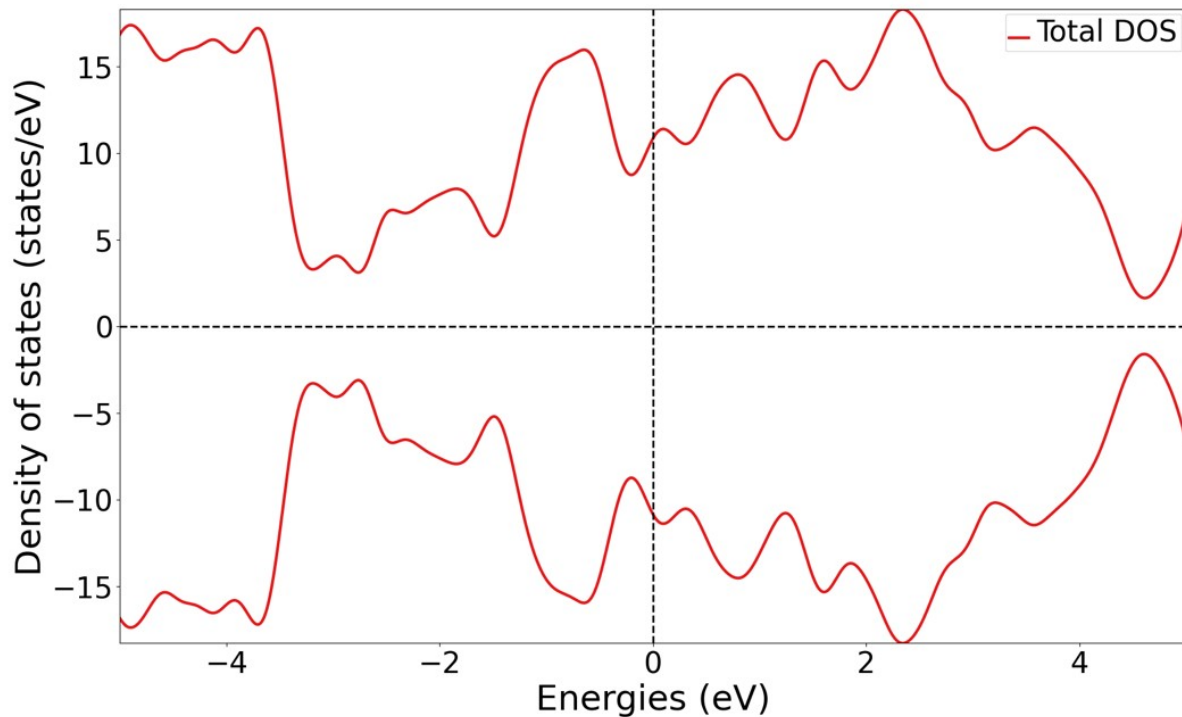


Figure S4. Density of states for Mo₂C-SAC.

As evident from these plots, the MXene-SAC motifs exhibit no band gap due to a continuous density of states around the Fermi level. We conclude that the metallic behavior of oxygen-covered MXene surfaces, as reported in previous works^{1,2}, remains unchanged despite the formation of the SAC-like structure.

Finally, we note that the MXene-SAC motif does not belong to the category of strongly correlated materials because the DOS peaks remain broad despite the formation of the SAC motif. This finding further justifies the chosen PBE+D3 level of theory (cf. Computational details in the main text), because the inclusion of the empirical Hubbard U term is only justified for strongly correlated materials or in the case of a bandgap material.

2 MXene-SAC structures

In the present work, we model the competition between the CER and OER on single atom centers of $p(3 \times 3)$ M₂CT_x(0001) and M₂NT_x(0001)MXenes with ABC stacking. While the terminal group, T_x, refers to a fully oxygen-covered surface, based on previous work by López *et al.*¹, the following seven metal atoms, M, are considered in our work: Ti, Zr, Hf, V, Nb, Ta, and Mo. Please note that some of the intermediate structures of Zr₂C and Mo₂C are distorted or unstable. Therefore, we exclude these two MXenes from the analysis and report activity and selectivity trends for the remaining 12 structures. Following our recent work, these MXenes form single-atom centers,

SAC-like sites, under anodic potential conditions [8] (cf. **Figure 1a** in the main text). However, it is important to note that, based on the application of *ab initio* molecular dynamics simulations, we observe that the SAC site can also be coordinated by more than a single adsorbate under anodic polarization. This is schematically illustrated in **Figure S5**, and in the present work we provide evidence that a two-branch coordination (cf. **Figure 1b** in the main text) refers to the energetically preferred active site motif under CER and OER conditions.

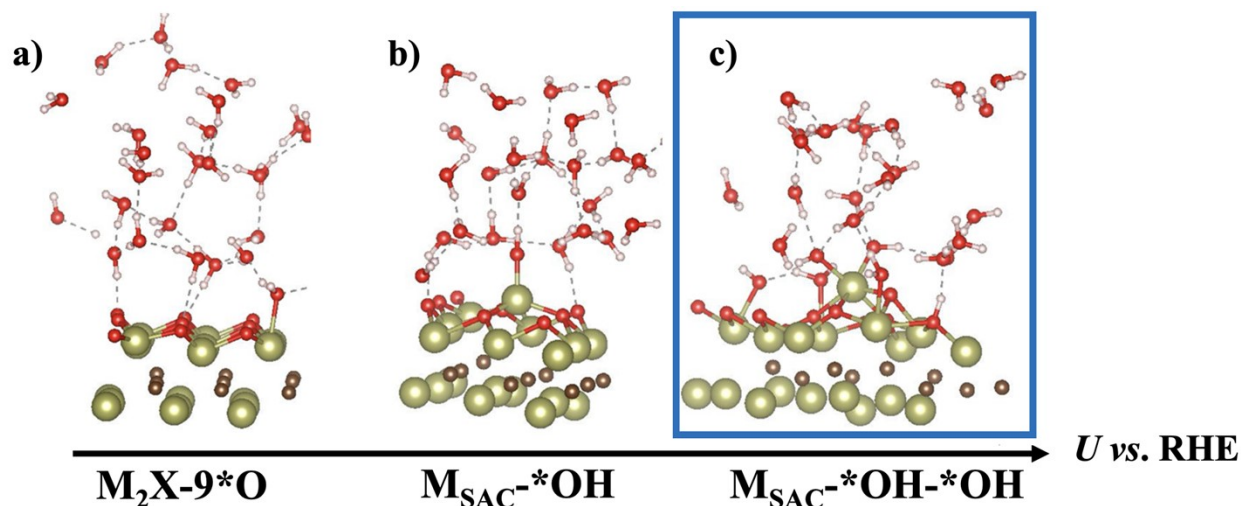
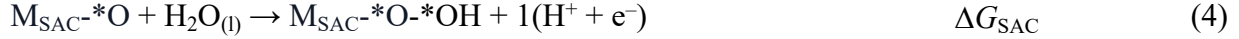


Figure S5. a) Pourbaix diagrams^{8,10} indicate that a fully oxygen-covered surface, M_2X-9*O , is the energetically preferred surface phase under CER and OER conditions. However, the static Pourbaix approach does not consider the dynamics of the electrolyte and an explicit electrode/electrolyte interaction. b) *Ab initio* molecular dynamics simulations reveal that MXenes form single-atom centers under anodic polarization (cf. **Figure 1a** in the main text). c) With increasing anodic bias, the formation of a two-branch MXene-SAC motif is observed (cf. **Figure 1b** in the main text). The two-branch MXene-SAC motif may represent the active phase in the CER and OER (cf. section 3 of the SI).

3 Thermodynamic analysis of MXene-SAC formation

In section 2 of the SI, we have discussed that the MXene surface reconstructs in the presence of an aqueous electrolyte, and the resulting surface structure with a metal atom out of plane is reminiscent of the coordination of a single-atom catalyst (cf. **Figure S5**). To this end, we refer to this motif as a SAC-like structure or MXene-SAC motif. While our previous work³ focused on the so-called one-branch MXene-SAC motif (cf. **Figure 1a** in the main text), in the following we provide evidence that the two-branch MXene-SAC motif (cf. **Figure 1b** in the main text) may correspond to the active phase under CER and OER conditions.

To determine the applied electrode potential at which the formation of the two-branch MXene-SAC motif becomes energetically favored over the one-branch MXene-SAC motif, we calculate the free-energy change for the formation of the two-branch MXene-SAC motif using the one-branch MXene-SAC motif as a reference structure:

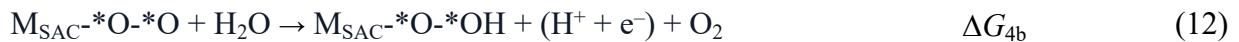
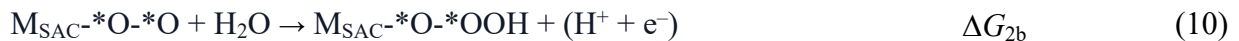
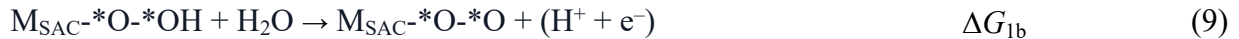
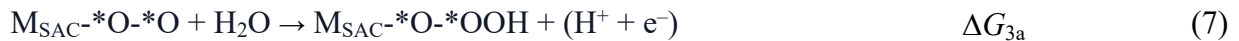


For all twelve $\text{M}_2\text{X}(0001)$ structures considered in this work (cf. section 2 of the SI), we determine ΔG_{SAC} using the CHE approach (cf. section 4 of the SI). Considering that for an oxidative process the scaling between free energy and applied electrode potential reads $nU = \Delta G$, where n indicates the number of electrons transferred (here $n = 1$), we calculate the applied electrode potential $U_{\text{eq}} = \Delta G_{\text{SAC}} / e$, at which the formation of the two-branch MXene-SAC motif becomes thermodynamically preferred. The results are shown in **Figure 2** of the main text, indicating that the two-branch MXene-SAC motif is formed at electrode potentials below the equilibrium potential of the OER. Therefore, we use the two-branch SAC structure to investigate the competition between the CER and OER through a combination of free-energy diagrams and a descriptor-based analysis.

4 Modeling the elementary steps of the OER and CER: the $G_{\text{max}}(U)$ descriptor

The elementary reaction steps of the OER and CER are given in equations (1) – (10) of the main text. We repeat them here for the sake of clarity.

The OER — $2 \text{H}_2\text{O} \rightarrow \text{O}_2 + 4 \text{H}^+ + 4 \text{e}^-$, $U_{\text{OER}}^0 = 1.23 \text{ V vs. RHE}$ (reversible hydrogen electrode) — is described by either the traditional mononuclear mechanism (cf. equations (5) – (8)) or by a Walden-type description⁴⁻⁶ including the $\eta_1\text{-*OO(H)}$ intermediate (cf. equations (9) – (12)). A schematic illustration of both reaction mechanisms is provided in **Figure 3** of the main text.



The free-energy changes of equations (5) – (12) are determined using the CHE approach. This implies that we rely on the equilibrium of equation (13) to relate the free energy of a proton-electron pair to half the free energy of a hydrogen molecule:



Note that the above equilibrium is met at $U = 0$ V vs. RHE (reversible hydrogen electrode), $T = 298.15$ K, and $p_{H_2} = 1$ atm. In addition, we use gaseous water at $T = 298.15$ K, and $p_{H_2O} = 0.035$ atm as a reference state, since water vapor and liquid water are in equilibrium under these conditions. The $\Delta G(0)$ values for the mononuclear and Walden-type mechanisms are summarized in **Table S1**.

Table S1. Free-energy changes, $\Delta G(0)$, of the OER intermediates via the mononuclear or the Walden-type description at $U = 0$ V vs. RHE.

MXene-SAC	ΔG_{1a} (eV)	ΔG_{2a} (eV)	ΔG_{3a} (eV)	ΔG_{4a} (eV)	ΔG_{1b} (eV)	ΔG_{2b} (eV)	ΔG_{3b} (eV)	ΔG_{4b} (eV)
Ti₂C	0.36	1.26	1.91	1.39	1.26	1.91	1.80	-0.05
Hf₂C	-1.23	0.68	3.66	1.81	0.67	3.66	-1.16	1.75
V₂C	0.75	0.72	2.40	1.05	0.72	2.40	1.22	0.58
Nb₂C	-0.34	0.69	2.82	1.75	0.69	2.82	1.11	0.30
Ta₂C	1.76	0.89	2.78	-0.51	0.89	2.78	1.24	0.01
Ti₂N	0.45	1.49	1.92	1.06	1.49	1.91	1.57	-0.05
Zr₂N	-0.02	1.95	1.59	1.40	1.95	1.59	1.65	-0.27
Hf₂N	-0.48	2.02	1.60	1.78	2.02	1.60	-0.72	2.02
V₂N	0.20	0.40	2.90	1.42	0.40	2.90	0.70	0.92
Nb₂N	-0.41	1.00	2.49	1.85	1.00	2.49	1.28	0.15
Ta₂N	-1.14	1.00	2.57	2.49	1.00	2.57	1.41	-0.06
Mo₂N	-0.81	0.87	2.53	2.33	0.87	2.53	1.37	0.15

To incorporate the applied electrode potential into the free-energy changes of **Table S1**, it is sufficient to count the number of transferred electrons, $\nu(e^-)$, in each adsorption process (cf. equations (5) – (12)). This leads to the introduction of potential-dependent free-energy changes, $\Delta G(U)$, based on the DFT-calculated $\Delta G(0)$ values:

$$\Delta G(U) = \Delta G(0) - \nu(e^-)eU \quad (14)$$

The potential-dependent free-energy changes are used to comprehend the electrocatalytic activity of the two-branch MXene-SAC motif in the OER. First, we note that the sum of the $\Delta G(U)$ values, independent of the mechanistic description, must satisfy the constraints imposed by equilibrium thermodynamics: at the OER equilibrium potential, $U_{\text{OER}} = 1.23$ V vs. RHE, the sum of the four free-energy changes is equal to zero. This is achieved by the consideration of gas-phase error corrections, as reported in previous works by Calle-Vallejo and coworkers^{7,8}.

Knowledge of the potential-dependent free-energy changes of the mononuclear and Walden-type mechanism enables determining the free energies of the reaction intermediates involved in both pathways. This is schematically shown for the mononuclear description:

Based on the free energies of the intermediate states, we determine the descriptor $G_{\max}^{\text{OER}}(U)^{9,10}$ for the mononuclear mechanism (cf. equations (15) – (20)). This is achieved by inspecting all possible free-energy spans between the intermediate states and by extracting the largest span at a given potential U :

$$G_{M_{\text{SAC}}^{-*}o}(U) = 0 \quad (15)$$

$$G_{M_{\text{SAC}}^{-*}o^{-*}oH}(U) = \Delta G_{1a} = \Delta G_{1a}^0 - eU \quad (16)$$

$$G_{M_{\text{SAC}}^{-*}o^{-*}o}(U) = \Delta G_{1a} + \Delta G_{2a} = \Delta G_{1a}^0 + \Delta G_{2a}^0 - 2eU \quad (17)$$

$$G_{M_{\text{SAC}}^{-*}o^{-*}oOH}(U) = \Delta G_{1a} + \Delta G_{2a} + \Delta G_{3a} = \Delta G_{1a}^0 + \Delta G_{2a}^0 + \Delta G_{3a}^0 - 3eU \quad (18)$$

$$G_{M_{\text{SAC}}^{-*}o + o_2}(U) = \sum_{i=1}^4 \Delta G_i = 4.92 - 4eU \quad (19)$$

$$\begin{aligned} G_{\max}^{\text{OER}}(U) = \max\{ & G_{M_{\text{SAC}}^{-*}o^{-*}oH}(U) - G_{M_{\text{SAC}}^{-*}o}(U); \\ & G_{M_{\text{SAC}}^{-*}o^{-*}o}(U) - G_{M_{\text{SAC}}^{-*}o}(U); \\ & G_{M_{\text{SAC}}^{-*}o^{-*}oOH}(U) - G_{M_{\text{SAC}}^{-*}o}(U); \\ & G_{M_{\text{SAC}}^{-*}o^{-*}o}(U) - G_{M_{\text{SAC}}^{-*}o^{-*}oH}(U); \\ & G_{M_{\text{SAC}}^{-*}o^{-*}oOH}(U) - G_{M_{\text{SAC}}^{-*}o^{-*}oH}(U); \\ & G_{M_{\text{SAC}}^{-*}o + o_2(g)}(U) - G_{M_{\text{SAC}}^{-*}o^{-*}oH}(U); \\ & G_{M_{\text{SAC}}^{-*}o^{-*}oOH}(U) - G_{M_{\text{SAC}}^{-*}o^{-*}o}(U); \\ & G_{M_{\text{SAC}}^{-*}o + o_2(g)}(U) - G_{M_{\text{SAC}}^{-*}o^{-*}o}(U) \} \\ & G_{M_{\text{SAC}}^{-*}o + o_2(g)}(U) - G_{M_{\text{SAC}}^{-*}o^{-*}oOH}(U) \} \end{aligned} \quad (20)$$

For the Walden-type mechanism, we follow the same type of analysis, which we do not repeat here. Instead, we refer to the literature for further discussion⁵. Consequently, we determine the descriptor $G_{\max}^{\text{OER}}(U)$ for all twelve M_2X -SAC motifs considered in this work using the mononuclear and Walden-type descriptions. The obtained values at $U = 1.40$ V vs. RHE are shown in **Figure 4** of the main text. Based on this comparison, we adopt the energetically favored mechanistic description for the OER for each M_2X -SAC structure, and the mechanism with the lower $G_{\max}^{\text{OER}}(U)$ value is used to quantify CER selectivity, as discussed below.

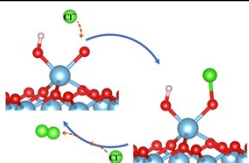
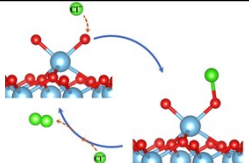
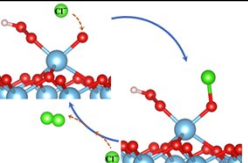
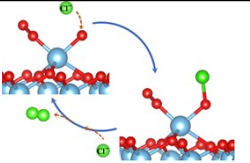
We exert the same approach to the theoretical description of the CER — $2\text{Cl}^- \rightarrow \text{Cl}_2 + 2e^-$, $U_{\text{OER}}^0 = 1.36$ V vs. SHE (standard hydrogen electrode) — which is assumed to proceed via the Volmer-Heyrovsky mechanism¹¹. For the sake of clarity, we repeat the mechanistic

descriptions from the main text in equations (21) – (22), where *X denotes an arbitrary OER intermediate:



We calculate the free-energy changes ΔG_{Vol} and ΔG_{Hey} using the CHE approach and a computational chlorine electrode, as described in previous works^{11–13}. **Table S2** summarizes the ΔG_{Vol} and ΔG_{Hey} values for the different active site motifs, which are visualized in **Figure 3** of the main text.

Table S2. Free-energy changes, $\Delta G(0)$, of the CER intermediates at $U = 0$ V vs. SHE and $\text{pH} = 0$. Note that this reference state is identical to the discussion of the OER energetics on the RHE scale. Inset side views of the elementary steps are shown, where M, O, H, and Cl atoms are indicated by blue, red, white, and green spheres, respectively.

Active site motif								
	ΔG_{Vol} (eV)	ΔG_{Hey} (eV)	ΔG_{Vol} (eV)	ΔG_{Hey} (eV)	ΔG_{Vol} (eV)	ΔG_{Hey} (eV)	ΔG_{Vol} (eV)	ΔG_{Hey} (eV)
MXene-SAC								
Ti₂C	1.40	1.32	0.08	2.64	1.22	1.50	2.10	0.62
Hf₂C	0.79	1.93	0.95	1.77	3.42	-2.98	-1.94	4.66
V₂C	2.07	0.65	1.04	1.68	1.90	0.82	1.44	1.28
Nb₂C	2.18	0.54	1.03	1.69	2.32	0.40	1.49	1.23
Ta₂C	2.28	0.44	1.13	1.59	2.32	0.40	1.57	1.15
Ti₂N	-0.39	3.11	1.02	1.70	1.34	1.38	1.16	1.56
Zr₂N	0.91	1.81	0.84	1.88	0.94	1.78	0.88	1.84
Hf₂N	0.83	1.89	-0.18	2.90	0.89	1.83	-1.64	4.36
V₂N	2.40	0.32	1.32	1.40	2.42	0.30	1.55	1.17
Nb₂N	1.95	0.77	0.87	1.85	2.02	0.70	1.34	1.38
Ta₂N	2.05	0.67	0.86	1.86	2.11	0.61	1.43	1.29
Mo₂N	-0.56	3.28	-0.11	2.83	-0.22	2.94	-0.12	2.84

Knowledge of ΔG_{Vol} and ΔG_{Hey} enables the determination of the descriptor $G_{\text{max}}^{\text{CER}}(U)$ in the same way as for the OER. **Table S3** provides an overview of the $G_{\text{max}}^{\text{OER}}(U)$ and $G_{\text{max}}^{\text{CER}}(U)$ values for the twelve different M_2X -SAC structures considered in this work at $U = 1.40$ V vs. RHE. There, we also report the determined CER selectivity based on the application of equations (11) – (12) of the main text.

Table S3. $G_{\max}^{\text{OER}}(U = 1.40 \text{ V})$ values for the different OER pathways as well as $G_{\max}^{\text{CER}}(U = 1.40 \text{ V})$ values and CER selectivity (cf. equation (11) – (12) of the main text).

MXene - SAC	$G_{\max}^{\text{OER}}(U)$		Motifs							
	Mono - nuclear	Mono - Walden	$\text{M}_{\text{SAC}}\text{-*O-*OH}$		$\text{M}_{\text{SAC}}\text{-*O-*O}$		$\text{M}_{\text{SAC}}\text{-*O-*OOH}$		$\text{M}_{\text{SAC}}\text{-*O-*OO}$	
			$G_{\max}^{\text{CER}}(U)$	CER sel.	$G_{\max}^{\text{CER}}(U)$	CER sel.	$G_{\max}^{\text{CER}}(U)$	CER sel.	$G_{\max}^{\text{CER}}(U)$	CER sel.
Ti_2C	0.51	0.91	0.00	1.00	1.24	0.00	0.10	1.00	0.70	0.00
Hf_2C	2.67	2.26	0.53	1.00	0.37	1.00	2.02	1.00	3.26	0.00
V_2C	1.00	1.00	0.67	1.00	0.28	1.00	0.50	1.00	0.04	1.00
Nb_2C	1.77	1.42	0.78	1.00	0.29	1.00	0.92	1.00	0.09	1.00
Ta_2C	1.38	1.38	0.88	1.00	0.19	1.00	0.92	1.00	0.17	1.00
Ti_2N	0.61	0.77	1.71	0.00	0.30	1.00	-0.02	1.00	0.16	1.00
Zr_2N	0.74	0.99	0.41	1.00	0.48	1.00	0.38	1.00	0.44	1.00
Hf_2N	1.20	0.82	0.49	1.00	1.50	0.00	0.43	1.00	2.96	0.00
V_2N	1.52	1.49	1.00	1.00	0.00	1.00	1.02	1.00	0.15	1.00
Nb_2N	1.54	1.09	0.55	1.00	0.45	1.00	0.62	1.00	-0.02	1.00
Ta_2N	2.26	1.18	0.65	1.00	0.46	1.00	0.71	1.00	0.03	1.00
Mo_2N	2.06	1.13	1.88	0.00	1.43	0.00	1.54	0.00	1.44	0.00

In this section, we summarize the free-energy diagrams of the OER and CER over two-branch MXene-SAC. The corresponding free-energy landscapes are constructed based on the data provided in **Tables S1-S3** in the previous section. While the energetics of the elementary steps in the OER and CER is displayed at $U = 1.40 \text{ V}$ vs. RHE (which is an identical reference state to $U = 1.40 \text{ V}$ vs. SHE, $\text{pH} = 0$), we provide a potential-dependent analysis of CER selectivity for all twelve motifs considered in this work (cf. panel c) in **Figure S6-S17**). Please note that the potential-dependent selectivity analysis does not alter the results reported at $U = 1.40 \text{ V}$ vs. RHE in **Figure 5** and does not affect the general trends discussed in this work. For an overview of the potential-dependent selectivity analysis, we refer to **Figure S18**.

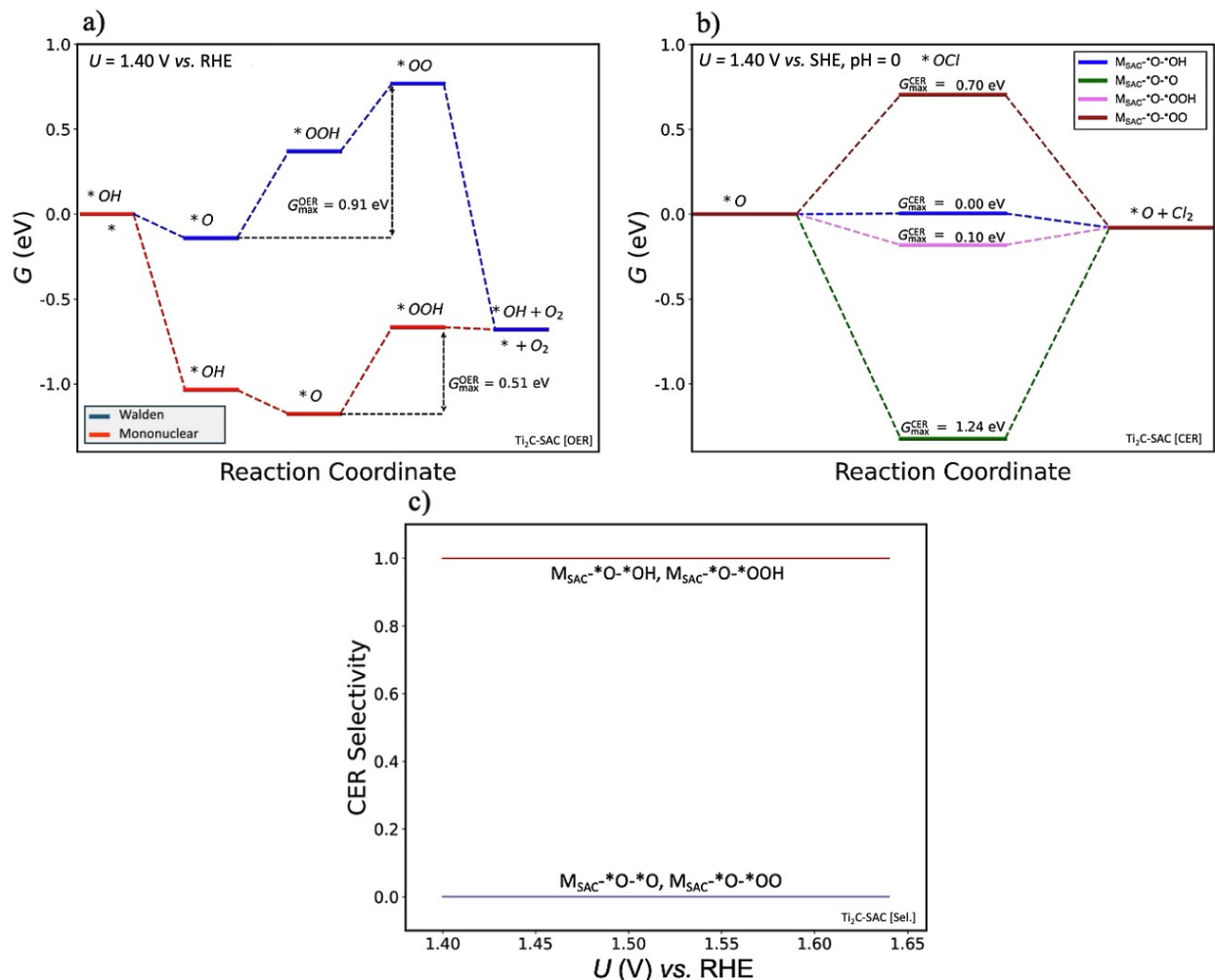


Figure S6. a) Free-energy diagram of the OER via the mononuclear or the Walden-type mechanism over two-branch $\text{Ti}_2\text{C-SAC}$ at $U = 1.40 \text{ V vs. RHE}$. We choose the pathway with the lower $G_{\text{max}}^{\text{OER}}(U)$ value for the description of the OER. **b)** Free-energy diagram of the CER via the Volmer-Heyrovsky mechanism at $U = 1.40 \text{ V vs. SHE, pH} = 0$. **c)** Based on the obtained $G_{\text{max}}^{\text{OER}}(U)$ and $G_{\text{max}}^{\text{CER}}(U)$ values, the CER selectivity (cf. equations (11) – (12) in the main text) is determined in a potential-dependent fashion.

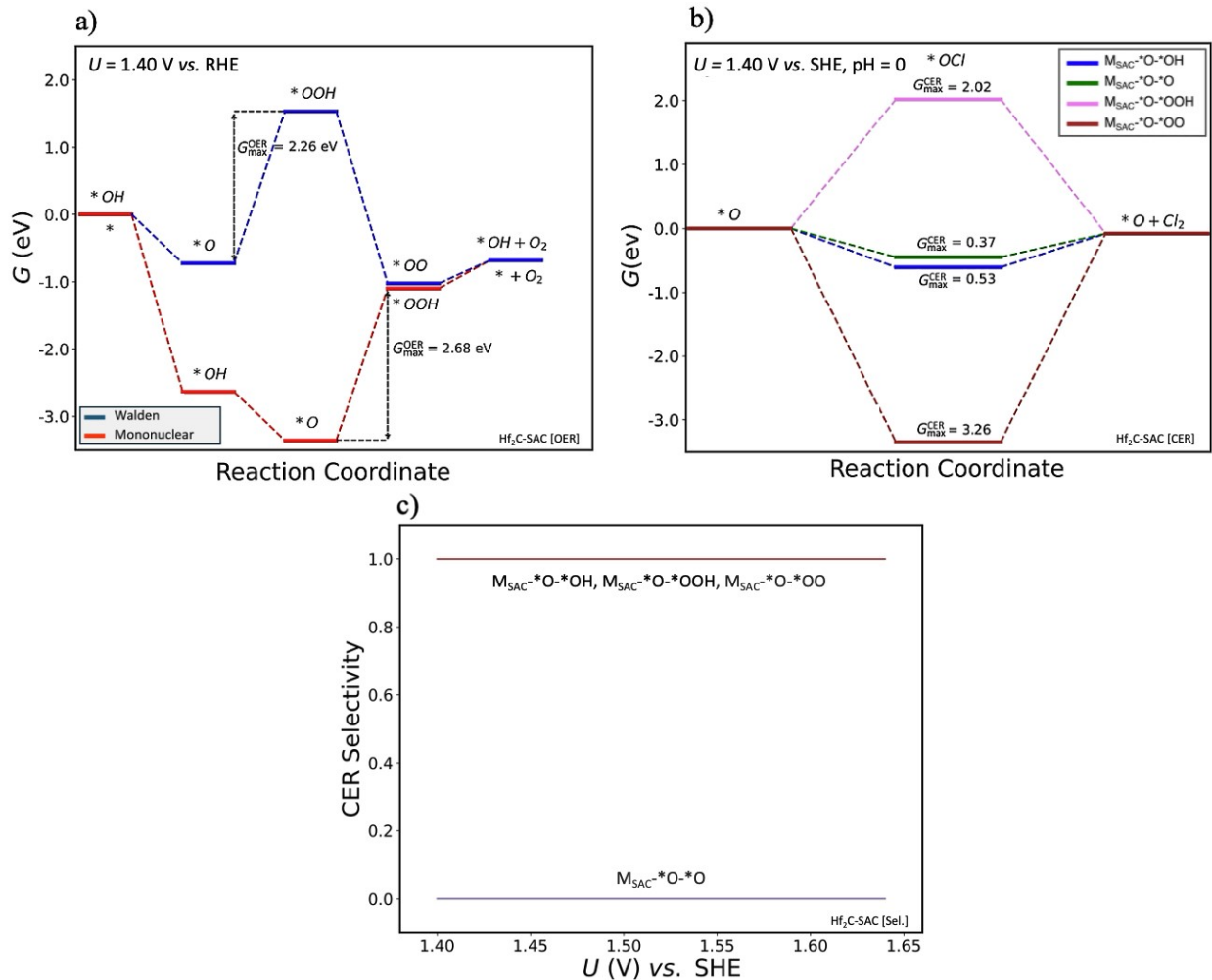


Figure S7. a) Free-energy diagram of the OER via the mononuclear or the Walden-type mechanism over two-branch Hf₂C-SAC at $U = 1.40$ V vs. RHE. We choose the pathway with the lower $G_{\max}^{\text{OER}}(U)$ value for the description of the OER. **b)** Free-energy diagram of the CER via the Volmer-Heyrovsky mechanism at $U = 1.40$ V vs. SHE, pH = 0. **c)** Based on the obtained $G_{\max}^{\text{OER}}(U)$ and $G_{\max}^{\text{CER}}(U)$ values, the CER selectivity (cf. equations (11) – (12) in the main text) is determined in a potential-dependent fashion.

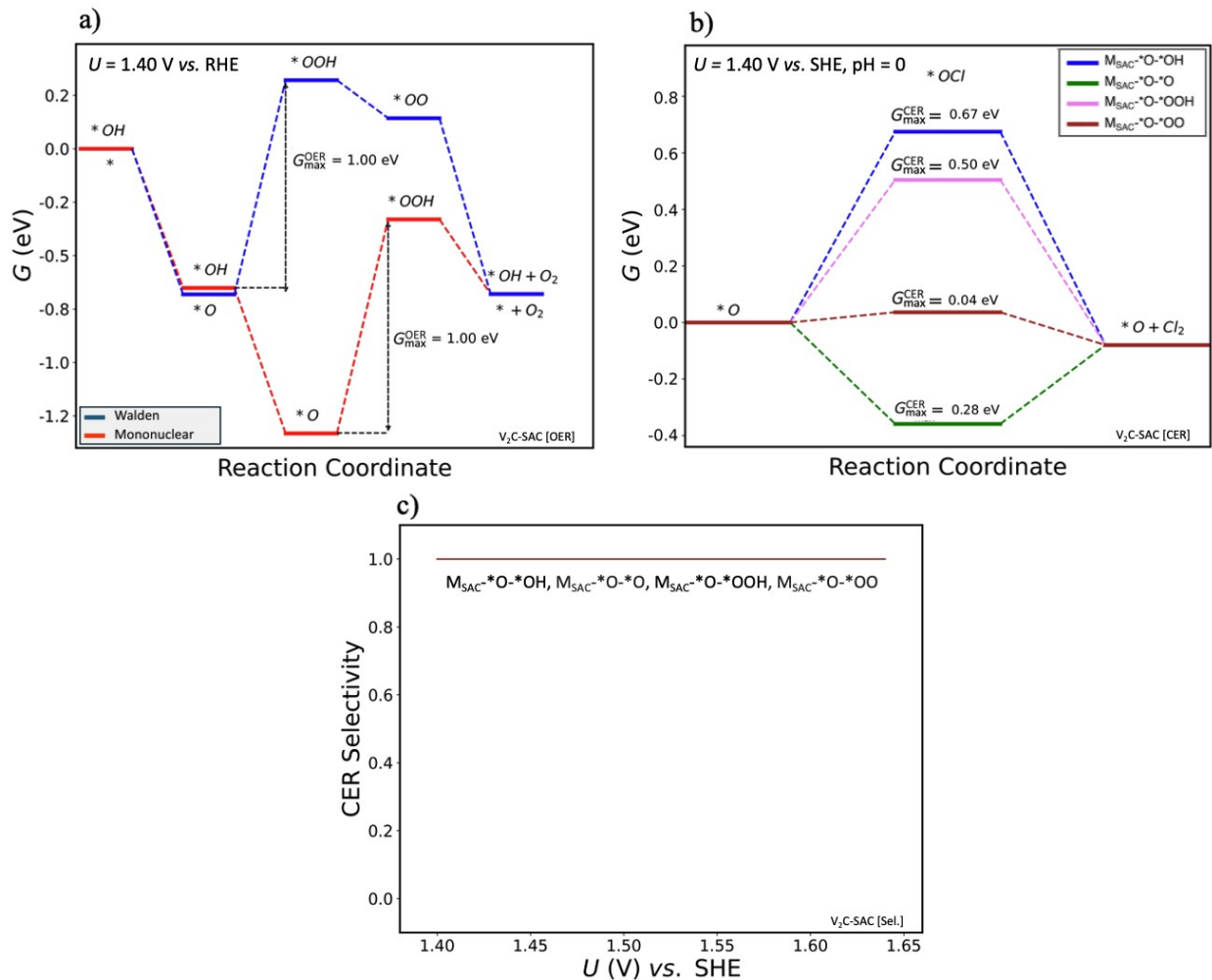


Figure S8. **a)** Free-energy diagram of the OER via the mononuclear or the Walden-type mechanism over two-branch V_2C -SAC at $U = 1.40$ V vs. RHE. We choose the pathway with the lower $G_{\max}^{\text{OER}}(U)$ value for the description of the OER. **b)** Free-energy diagram of the CER via the Volmer-Heyrovsky mechanism at $U = 1.40$ V vs. SHE, pH = 0. **c)** Based on the obtained $G_{\max}^{\text{OER}}(U)$ and $G_{\max}^{\text{CER}}(U)$ values, the CER selectivity (cf. equations (11) – (12) in the main text) is determined in a potential-dependent fashion.

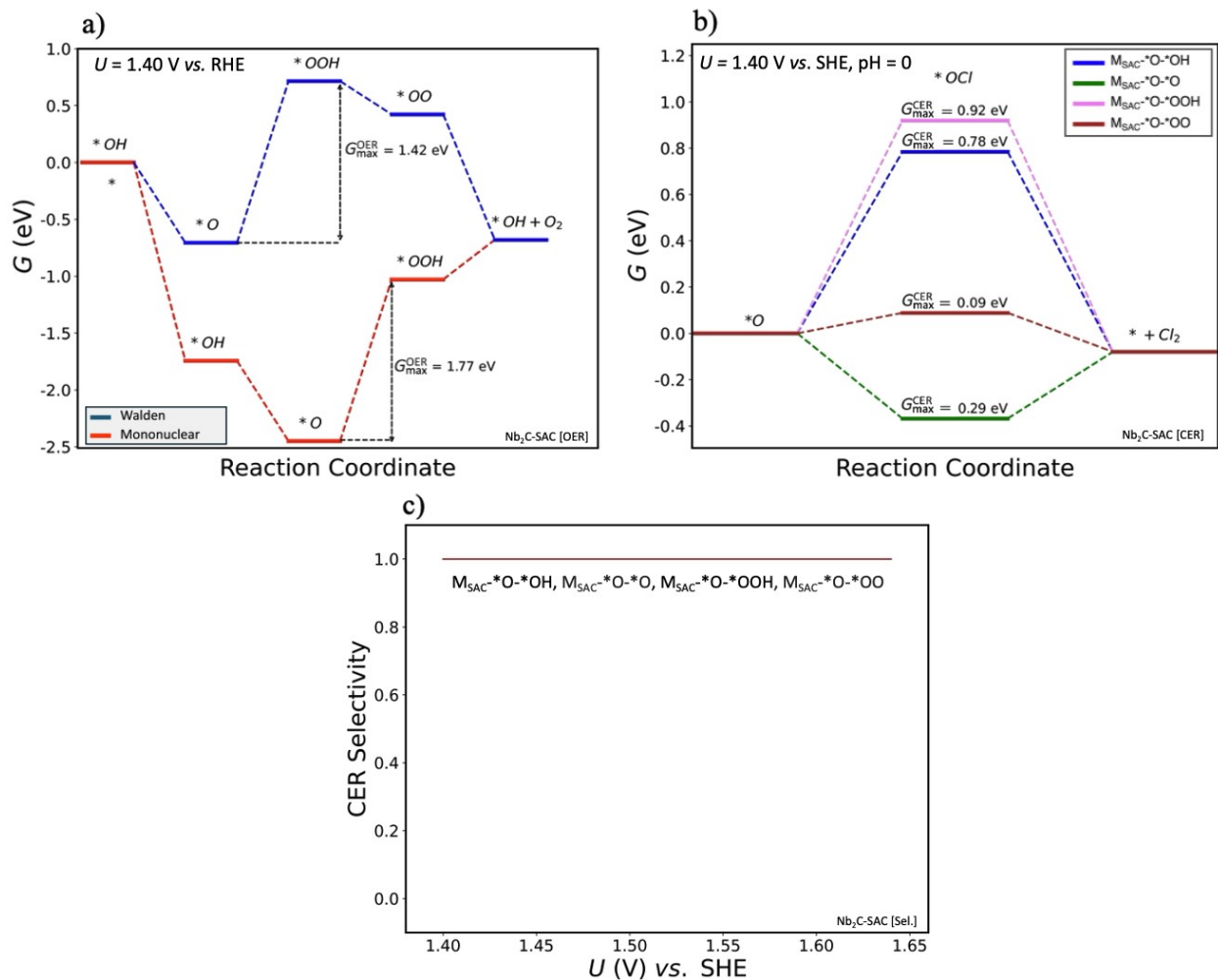


Figure S9. **a)** Free-energy diagram of the OER via the mononuclear or the Walden-type mechanism over two-branch $\text{Nb}_2\text{C-SAC}$ at $U = 1.40$ V vs. RHE. We choose the pathway with the lower $G_{\text{max}}^{\text{OER}}(U)$ value for the description of the OER. **b)** Free-energy diagram of the CER via the Volmer-Heyrovsky mechanism at $U = 1.40$ V vs. SHE, pH = 0. **c)** Based on the obtained $G_{\text{max}}^{\text{OER}}(U)$ and $G_{\text{max}}^{\text{CER}}(U)$ values, the CER selectivity (cf. equations (11) – (12) in the main text) is determined in a potential-dependent fashion.

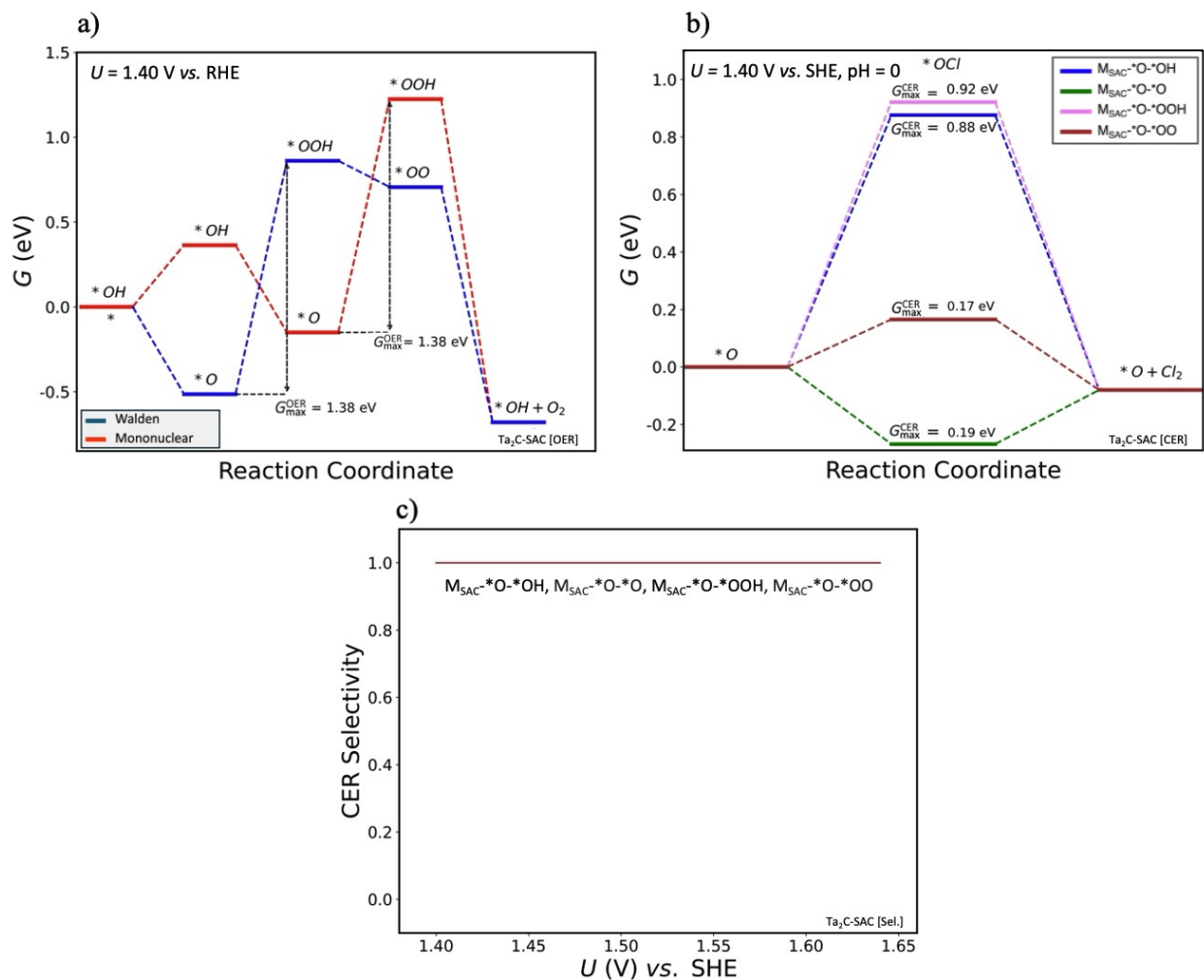


Figure S10. a) Free-energy diagram of the OER via the mononuclear or the Walden-type mechanism over two-branch $\text{Ta}_2\text{C-SAC}$ at $U = 1.40$ V vs. RHE. We choose the pathway with the lower $G_{\text{max}}^{\text{OER}}(U)$ value for the description of the OER. **b)** Free-energy diagram of the CER via the Volmer-Heyrovsky mechanism at $U = 1.40$ V vs. SHE, pH = 0. **c)** Based on the obtained $G_{\text{max}}^{\text{OER}}(U)$ and $G_{\text{max}}^{\text{CER}}(U)$ values, the CER selectivity (cf. equations (11) – (12) in the main text) is determined in a potential-dependent fashion.

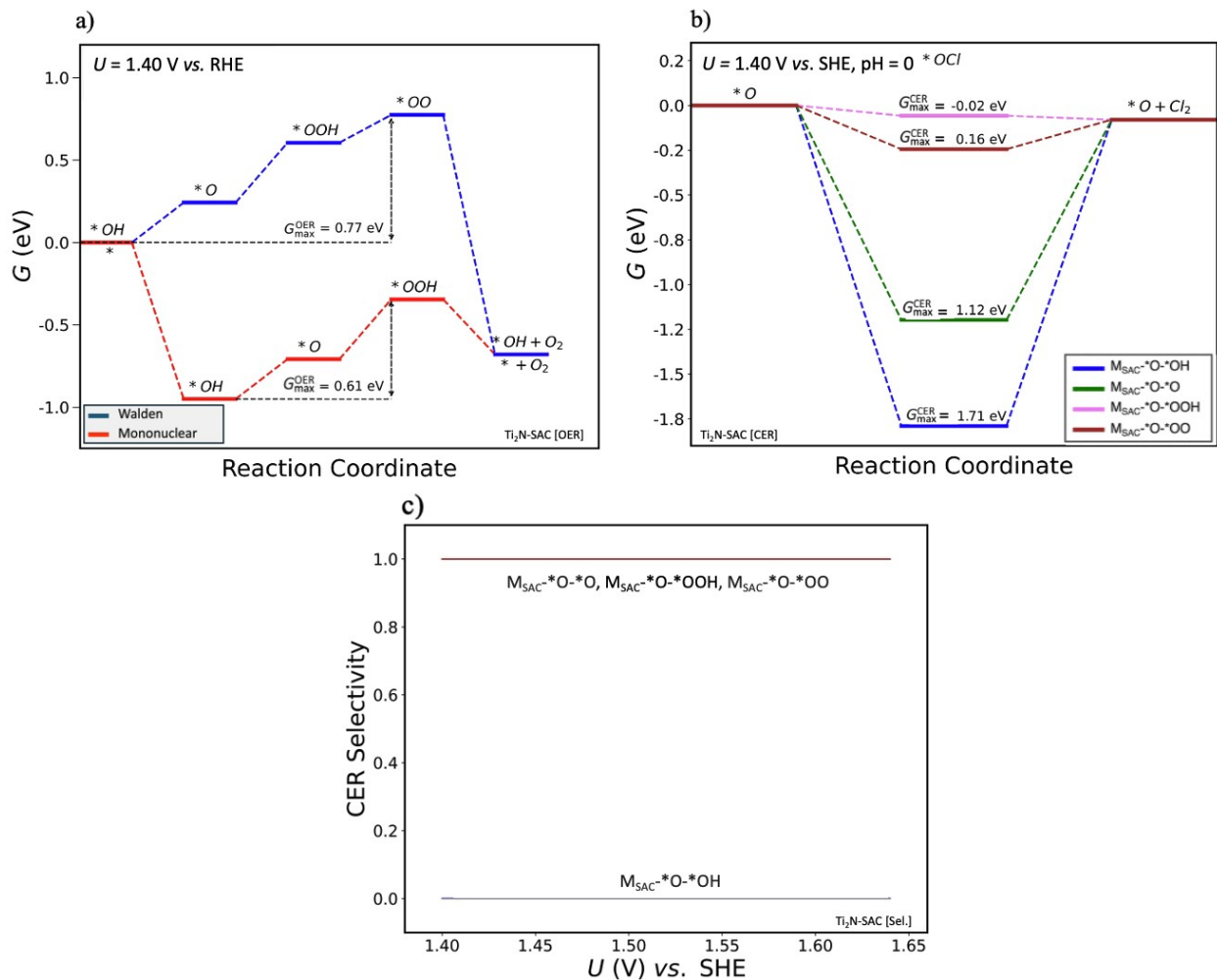


Figure S11. a) Free-energy diagram of the OER via the mononuclear or the Walden-type mechanism over two-branch $\text{Ti}_2\text{N-SAC}$ at $U = 1.40$ V vs. RHE. We choose the pathway with the lower $G_{\text{max}}^{\text{OER}}(U)$ value for the description of the OER. **b)** Free-energy diagram of the CER via the Volmer-Heyrovsky mechanism at $U = 1.40$ V vs. SHE, pH = 0. **c)** Based on the obtained $G_{\text{max}}^{\text{OER}}(U)$ and $G_{\text{max}}^{\text{CER}}(U)$ values, the CER selectivity (cf. equations (11) – (12) in the main text) is determined in a potential-dependent fashion.

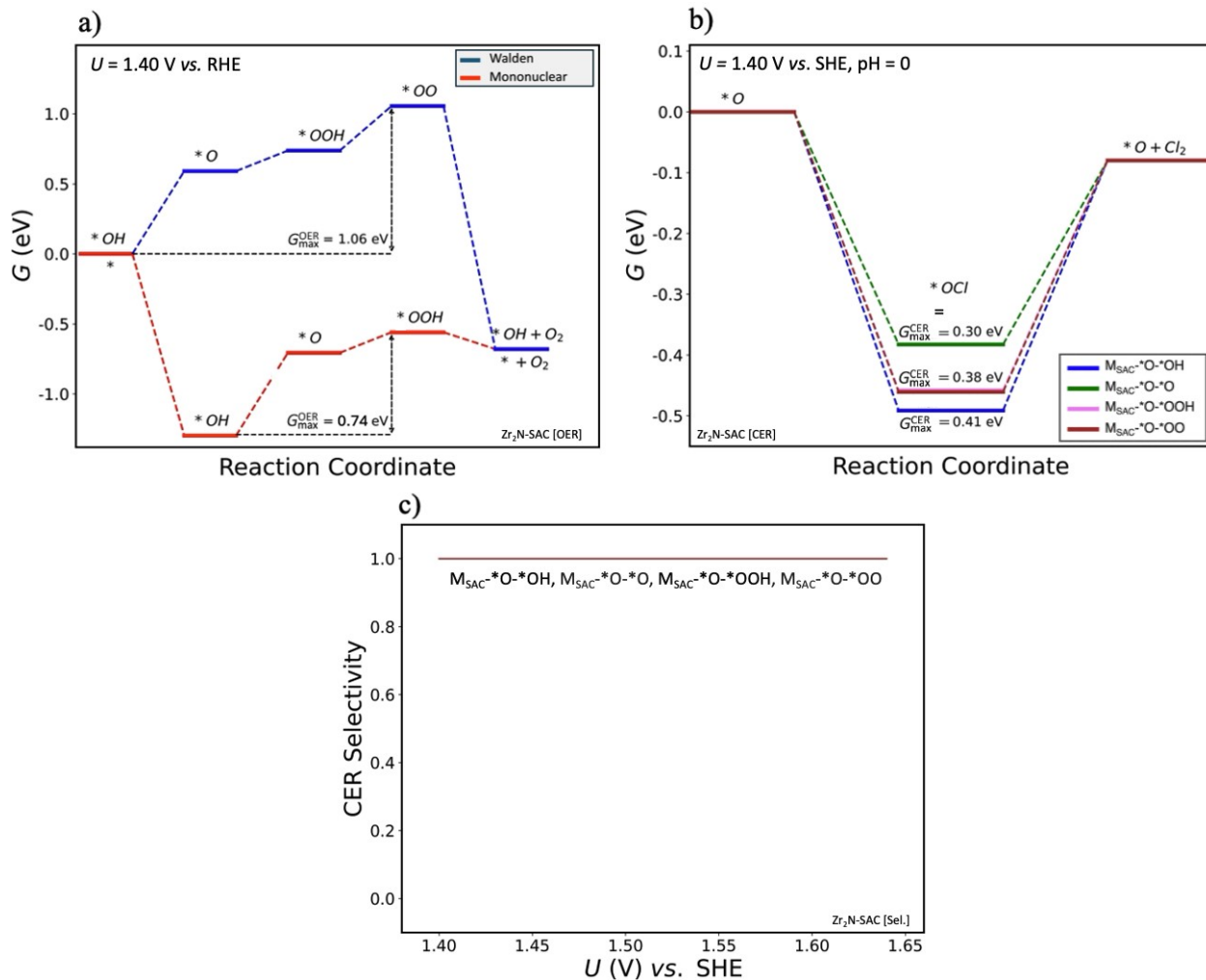


Figure S12. a) Free-energy diagram of the OER via the mononuclear or the Walden-type mechanism over two-branch $\text{Zr}_2\text{N-SAC}$ at $U = 1.40$ V vs. RHE. We choose the pathway with the lower $G_{\text{max}}^{\text{OER}}(U)$ value for the description of the OER. **b)** Free-energy diagram of the CER via the Volmer-Heyrovsky mechanism at $U = 1.40$ V vs. SHE, pH = 0. **c)** Based on the obtained $G_{\text{max}}^{\text{OER}}(U)$ and $G_{\text{max}}^{\text{CER}}(U)$ values, the CER selectivity (cf. equations (11) – (12) in the main text) is determined in a potential-dependent fashion.

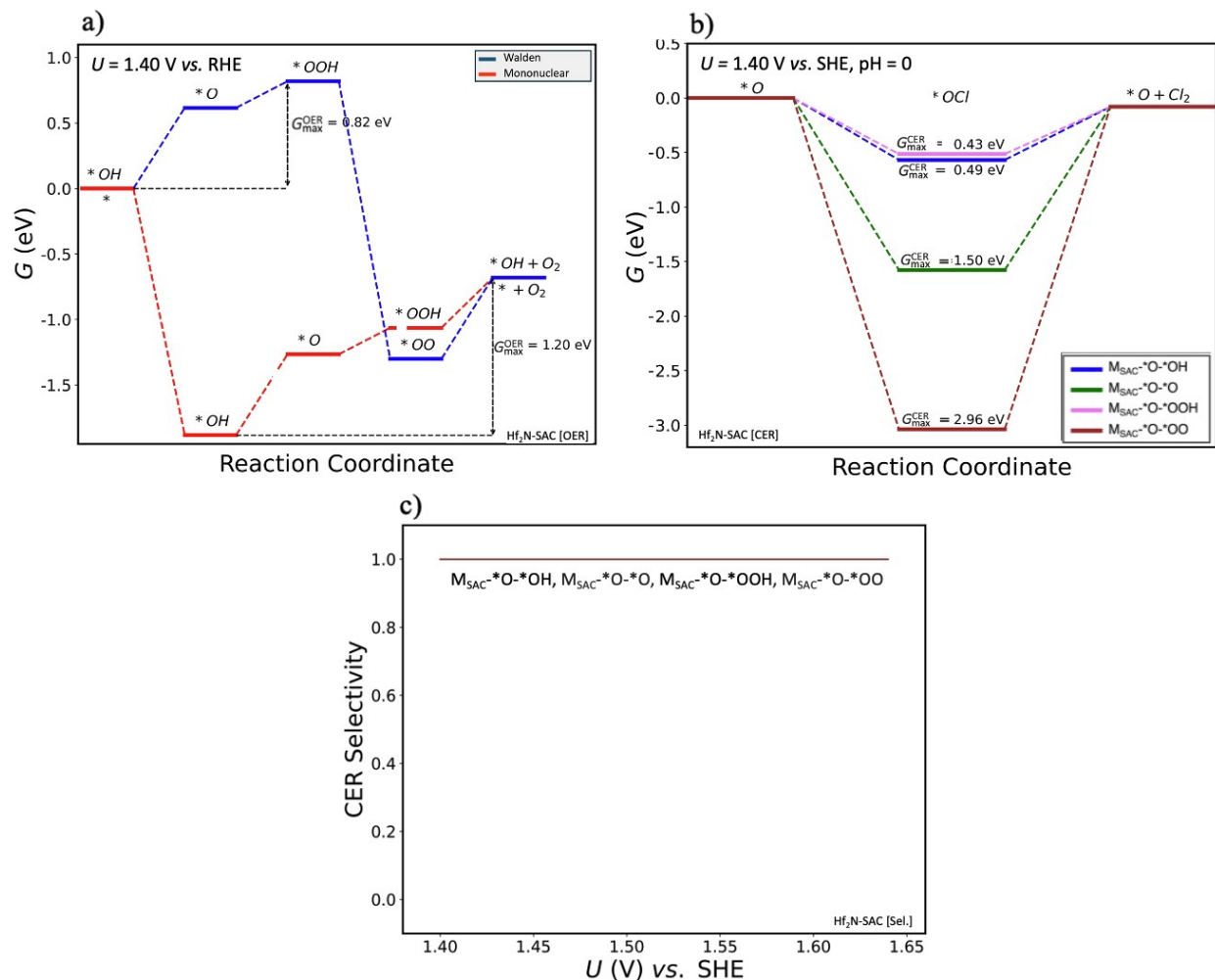


Figure S13. **a)** Free-energy diagram of the OER via the mononuclear or the Walden-type mechanism over two-branch $\text{Hf}_2\text{N-SAC}$ at $U = 1.40$ V vs. RHE. We choose the pathway with the lower $G_{\text{max}}^{\text{OER}}(U)$ value for the description of the OER. **b)** Free-energy diagram of the CER via the Volmer-Heyrovsky mechanism at $U = 1.40$ V vs. SHE, pH = 0. **c)** Based on the obtained $G_{\text{max}}^{\text{OER}}(U)$ and $G_{\text{max}}^{\text{CER}}(U)$ values, the CER selectivity (cf. equations (11) – (12) in the main text) is determined in a potential-dependent fashion.

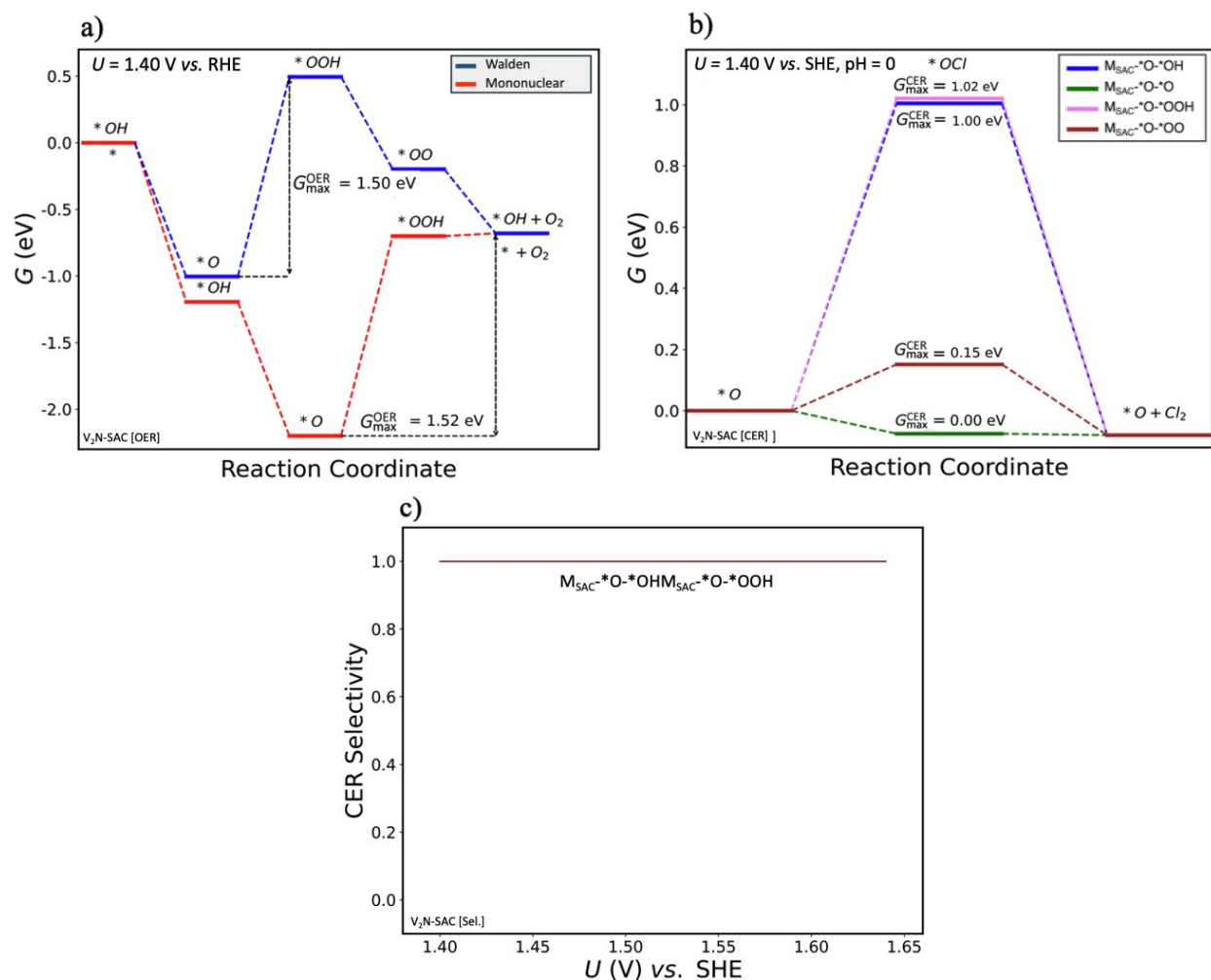


Figure S14. **a)** Free-energy diagram of the OER via the mononuclear or the Walden-type mechanism over two-branch V_2N -SAC at $U = 1.40$ V vs. RHE. We choose the pathway with the lower $G_{\max}^{\text{OER}}(U)$ value for the description of the OER. **b)** Free-energy diagram of the CER via the Volmer-Heyrovsky mechanism at $U = 1.40$ V vs. SHE, pH = 0. **c)** Based on the obtained $G_{\max}^{\text{OER}}(U)$ and $G_{\max}^{\text{CER}}(U)$ values, the CER selectivity (cf. equations (11) – (12) in the main text) is determined in a potential-dependent fashion.

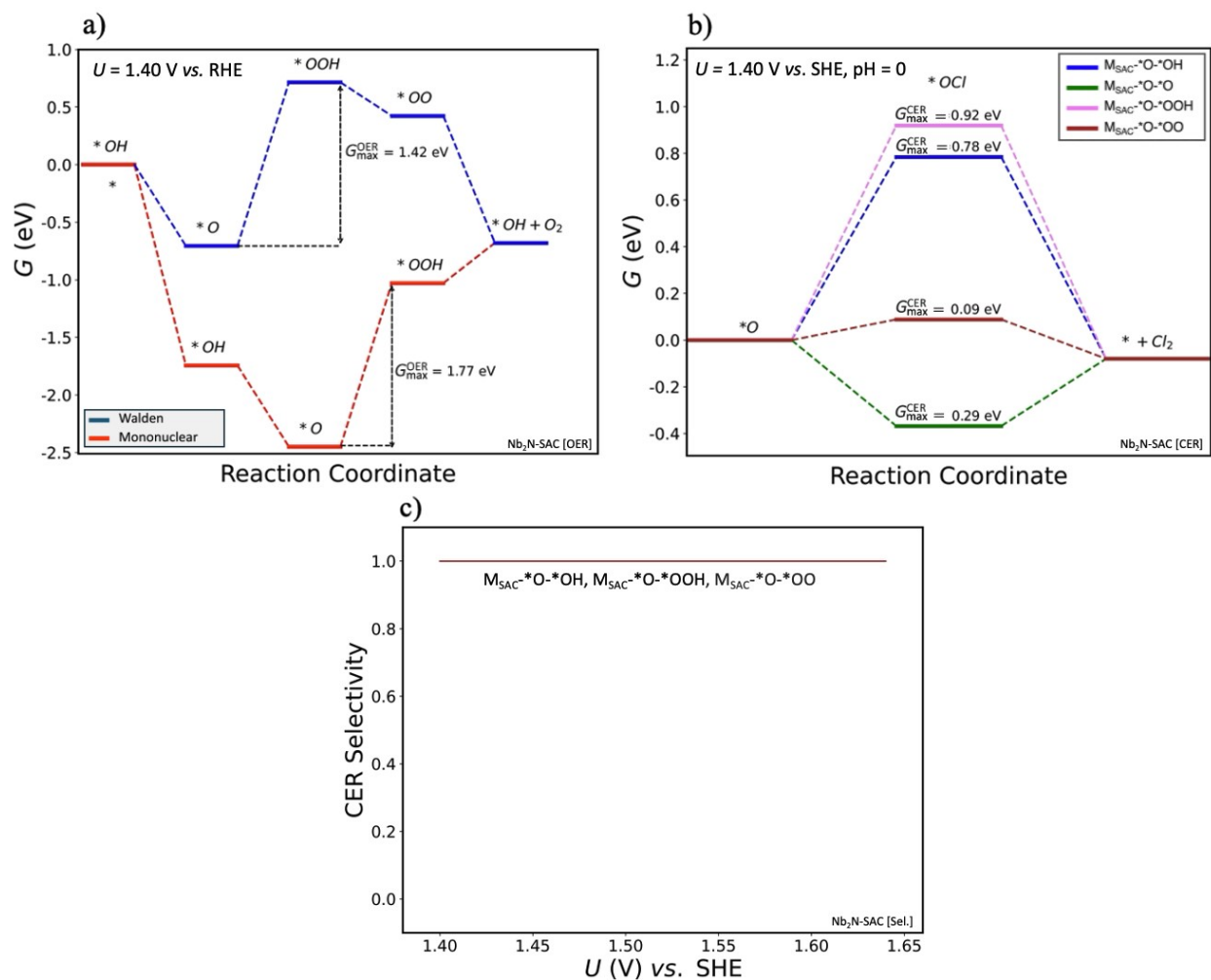


Figure S15. a) Free-energy diagram of the OER via the mononuclear or the Walden-type mechanism over two-branch $\text{Nb}_2\text{N-SAC}$ at $U = 1.40 \text{ V vs. RHE}$. We choose the pathway with the lower $G_{\text{max}}^{\text{OER}}(U)$ value for the description of the OER. **b)** Free-energy diagram of the CER via the Volmer-Heyrovsky mechanism at $U = 1.40 \text{ V vs. SHE, pH} = 0$.

c) Based on the obtained $G_{\text{max}}^{\text{OER}}(U)$ and $G_{\text{max}}^{\text{CER}}(U)$ values, the CER selectivity (cf. equations (11) – (12) in the main text) is determined in a potential-dependent fashion.

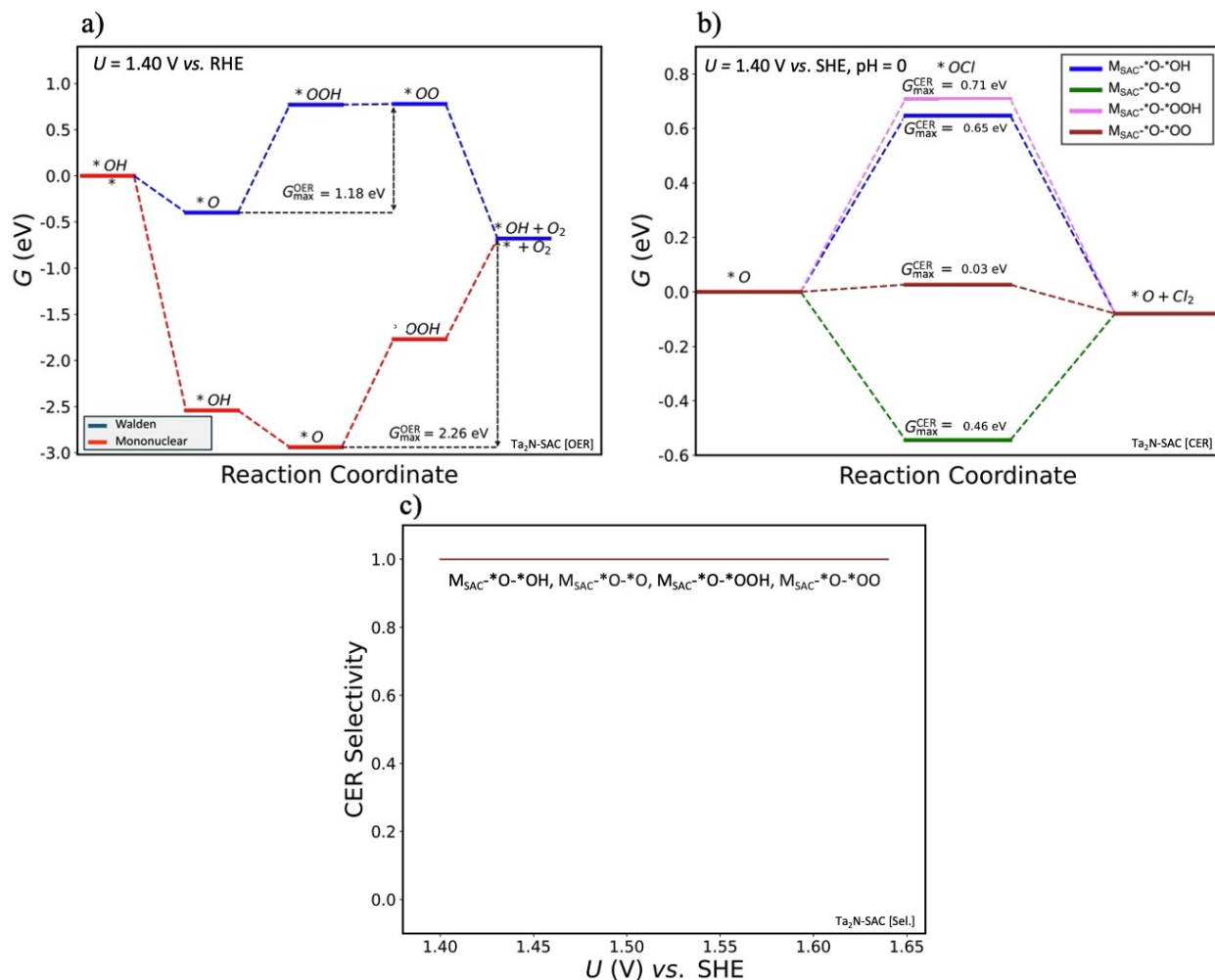


Figure S16. **a)** Free-energy diagram of the OER via the mononuclear or the Walden-type mechanism over two-branch $\text{Ta}_2\text{N-SAC}$ at $U = 1.40$ V vs. RHE. We choose the pathway with the lower $G_{\text{max}}^{\text{OER}}(U)$ value for the description of the OER. **b)** Free-energy diagram of the CER via the Volmer-Heyrovsky mechanism at $U = 1.40$ V vs. SHE, pH = 0. **c)** Based on the obtained $G_{\text{max}}^{\text{OER}}(U)$ and $G_{\text{max}}^{\text{CER}}(U)$ values, the CER selectivity (cf. equations (11) – (12) in the main text) is determined in a potential-dependent fashion.

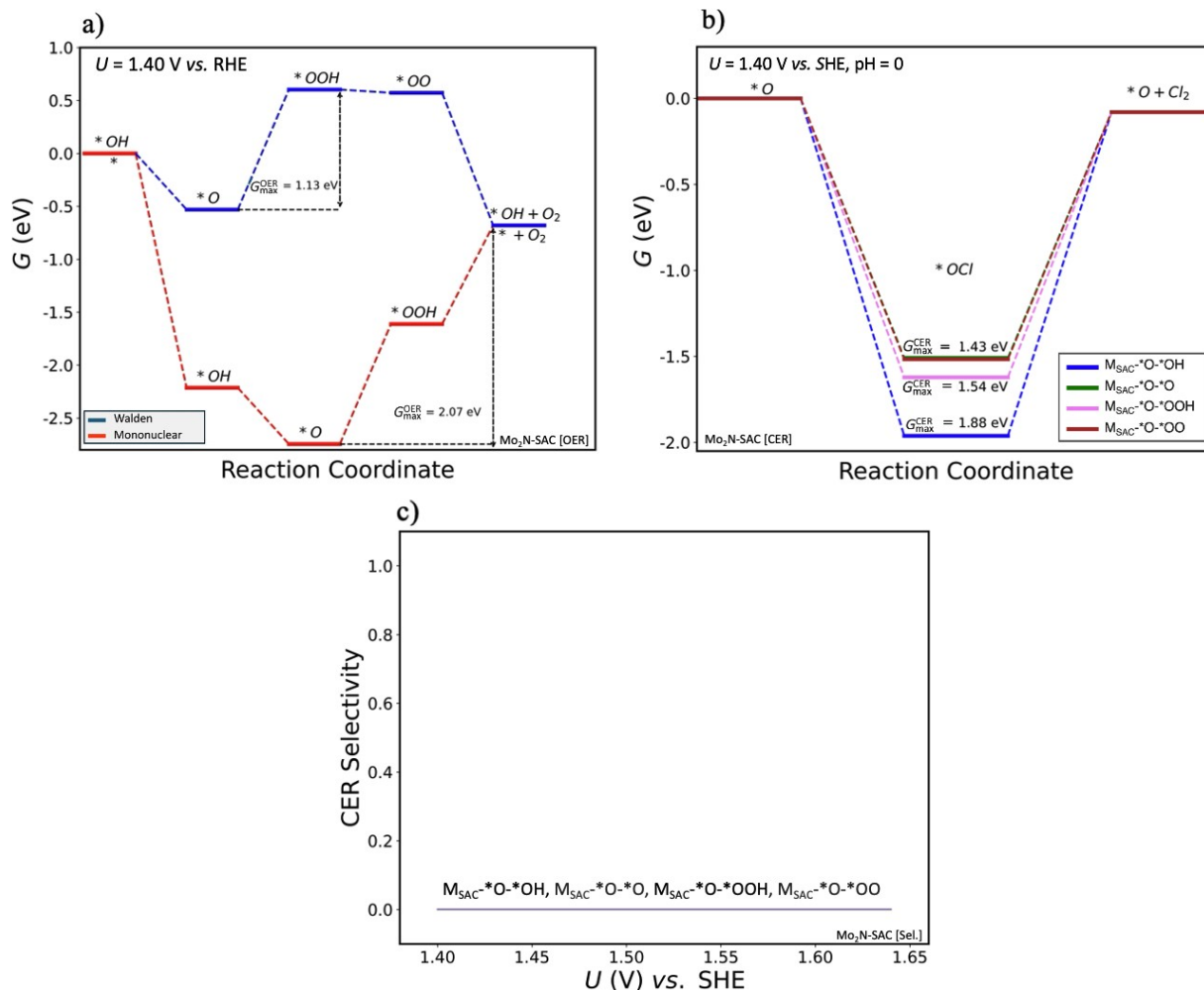


Figure S17. a) Free-energy diagram of the OER via the mononuclear or the Walden-type mechanism over two-branch Mo₂N-SAC at $U = 1.40$ V vs. RHE. We choose the pathway with the lower $G_{\text{max}}^{\text{OER}}(U)$ value for the description of the OER. **b)** Free-energy diagram of the CER via the Volmer-Heyrovsky mechanism at $U = 1.40$ V vs. SHE, pH = 0.

c) Based on the obtained $G_{\text{max}}^{\text{OER}}(U)$ and $G_{\text{max}}^{\text{CER}}(U)$ values, the CER selectivity (cf. equations (11) – (12) in the main text) is determined in a potential-dependent fashion.

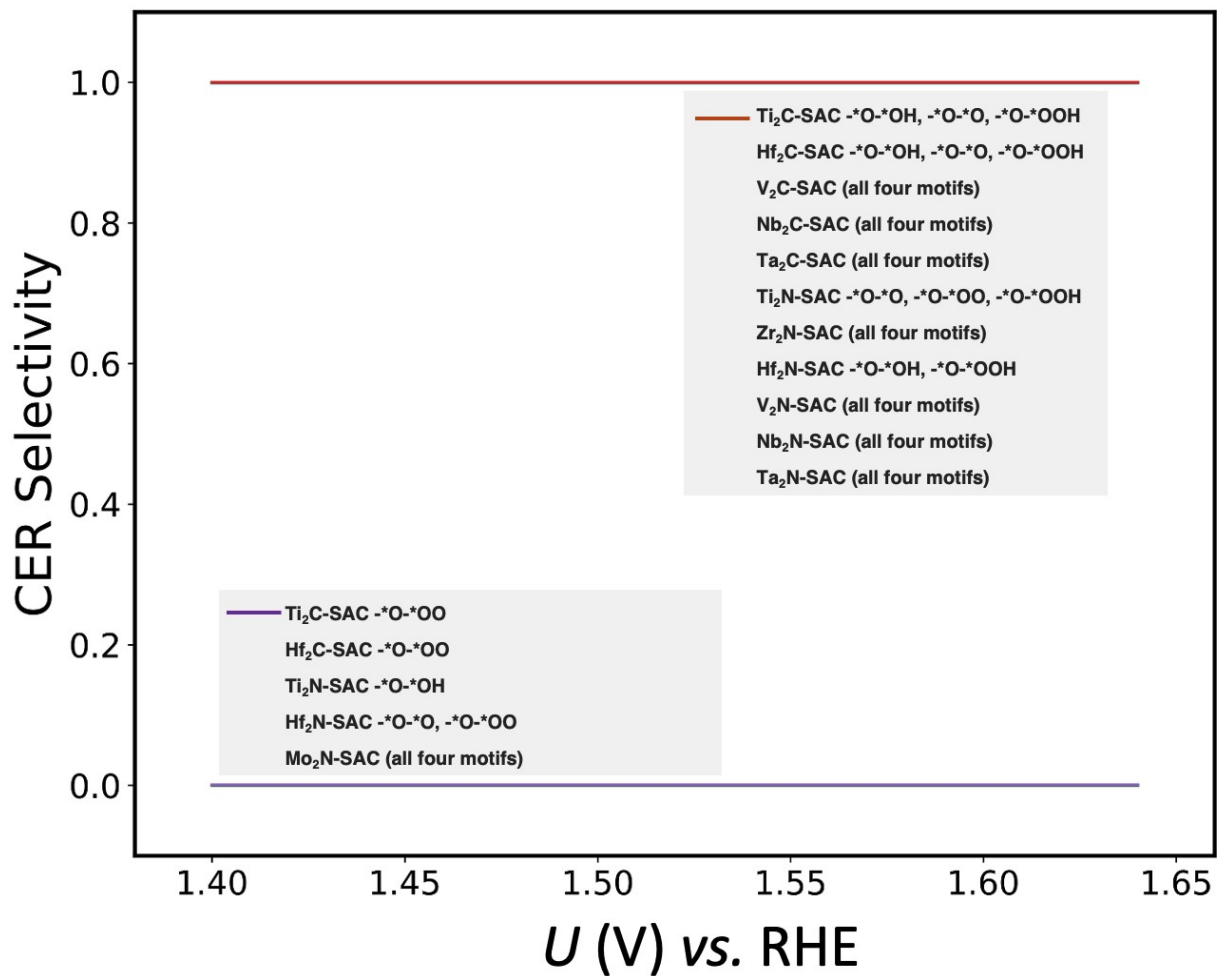


Figure S18. CER selectivity in dependence of the applied electrode potential for all 48 motifs of M_2X -SAC considered in this work.

References

- (1) López, M.; Exner, K. S.; Viñes, F.; Illas, F. Computational Pourbaix Diagrams for MXenes: A Key Ingredient toward Proper Theoretical Electrocatalytic Studies. *Advcd Theory and Sims* **2023**, *6* (10), 2200217. <https://doi.org/10.1002/adts.202200217>.
- (2) Razzaq, S.; Faridi, S.; Kenmoe, S.; Usama, M.; Singh, D.; Meng, L.; Vines, F.; Illas, F.; Exner, K. S. MXenes Spontaneously Form Active and Selective Single-Atom Centers under Anodic Polarization Conditions. *J. Am. Chem. Soc.* **2025**, *147* (1), 161–168. <https://doi.org/10.1021/jacs.4c08518>.
- (3) Razzaq, S.; Faridi, S.; Kenmoe, S.; Usama, M.; Singh, D.; Meng, L.; Vines, F.; Illas, F.; Exner, K. S. MXenes Spontaneously Form Active and Selective Single-Atom Centers under Anodic Polarization Conditions. *J. Am. Chem. Soc.* **2024**, *jacs.4c08518*. <https://doi.org/10.1021/jacs.4c08518>.
- (4) Yu, S.; Levell, Z.; Jiang, Z.; Zhao, X.; Liu, Y. What Is the Rate-Limiting Step of Oxygen Reduction Reaction on Fe–N–C Catalysts? *J. Am. Chem. Soc.* **2023**, *145* (46), 25352–25356. <https://doi.org/10.1021/jacs.3c09193>.
- (5) Exner, K. S. Importance of the Walden Inversion for the Activity Volcano Plot of Oxygen Evolution. *Advanced Science* **2023**, *10* (36), 2305505. <https://doi.org/10.1002/advs.202305505>.
- (6) Exner, K. S. Four Generations of Volcano Plots for the Oxygen Evolution Reaction: Beyond Proton-Coupled Electron Transfer Steps? *Acc. Chem. Res.* **2024**, *57* (9), 1336–1345. <https://doi.org/10.1021/acs.accounts.4c00048>.
- (7) Urrego-Ortiz, R.; Builes, S.; Illas, F.; Calle-Vallejo, F. Gas-Phase Errors in Computational Electrocatalysis: A Review. *EES. Catal.* **2024**, *2* (1), 157–179. <https://doi.org/10.1039/D3EY00126A>.
- (8) Granda-Marulanda, L. P.; Rendón-Calle, A.; Builes, S.; Illas, F.; Koper, M. T. M.; Calle-Vallejo, F. A Semiempirical Method to Detect and Correct DFT-Based Gas-Phase Errors and Its Application in Electrocatalysis. *ACS Catal.* **2020**, *10* (12), 6900–6907. <https://doi.org/10.1021/acscatal.0c01075>.
- (9) Exner, K. S. A Universal Descriptor for the Screening of Electrode Materials for Multiple-Electron Processes: Beyond the Thermodynamic Overpotential. *ACS Catal.* **2020**, *10* (21), 12607–12617. <https://doi.org/10.1021/acscatal.0c03865>.
- (10) Razzaq, S.; Exner, K. S. Materials Screening by the Descriptor $G_{\max}(\eta)$: The Free-Energy Span Model in Electrocatalysis. *ACS Catal.* **2023**, *13* (3), 1740–1758. <https://doi.org/10.1021/acscatal.2c03997>.
- (11) Hansen, H. A.; Man, I. C.; Studt, F.; Abild-Pedersen, F.; Bligaard, T.; Rossmeisl, J. Electrochemical Chlorine Evolution at Rutile Oxide (110) Surfaces. *Phys. Chem. Chem. Phys.* **2010**, *12* (1), 283–290. <https://doi.org/10.1039/B917459A>.
- (12) Exner, K. S.; Anton, J.; Jacob, T.; Over, H. Chlorine Evolution Reaction on RuO₂(110): Ab Initio Atomistic Thermodynamics Study - Pourbaix Diagrams. *Electrochimica Acta* **2014**, *120*, 460–466. <https://doi.org/10.1016/j.electacta.2013.11.027>.
- (13) Exner, K. S.; Anton, J.; Jacob, T.; Over, H. Controlling Selectivity in the Chlorine Evolution Reaction over RuO₂-Based Catalysts. *Angew. Chem. Int. Ed.* **2014**, *53* (41), 11032–11035. <https://doi.org/10.1002/anie.201406112>.